geosciences

MDPI

Article

Wrench Faults Trigger Geologic Emissions of Subterranean Gases

Dengliang Gao

Department of Geology and Geography, West Virginia University, Morgantown, WV 26506, USA; dengliang.gao@mail.wvu.edu

Abstract

Anthropogenic emissions of surface and near-surface gases have been widely recognized as the dominant forcing of global environmental changes; however, geologic emissions of deeply buried subterranean gases have not been well documented, where the causal mechanism of geologic emissions remains elusive. The biases towards anthropogenic emissions have limited the vision of the entire picture of underlying mechanisms of global environmental changes. Using greenhouse gas methane (CH_4) and radioactive gas radon (R_n) as examples, here I report observations and interpretations of wrench fault-related gas emissions. Subsurface remote sensing from global gas basins demonstrates a strong correlation of wrench faults to basin-scale methane leakage and venting. Surface monitoring of radon gas shows that gas fluxes could be highly concentrated on active wrench faults. The observations lead to a hypothetical conceptual model that wrench faults could act as most effective emission pathways due to their parallelism to buoyant force and lithostatic stress. The conceptual model of gas emission systems could be applicable in subsurface energy systems to explain the previously reported correlations of wrench faults to major discoveries of energy resources. My findings unravel the intricate interplay between emission and energy systems, thus providing a framework to bridge the gap between environmental integrity and energy security.

Keywords: geologic emissions; wrench faults; gas basins; subsurface remote sensing; surface monitoring; reduced-order modeling; environmental integrity; energy security

1. Introduction

Although it is relatively simple and easy to measure the concentrations of environmentally harmful gases saturated in surface waters, sediments, and air, it is challenging to pinpoint the root sources of the emitted gases and to partition the composite forcing of environmental changes. Anthropogenic gas emissions generated in the downstream of fossil fuel exploitation have been widely and conveniently regarded as the dominant driver of global environmental changes [1,2]. In turn, global warming feedback has been commonly regarded as being responsible for near-surface naturogenic gas emissions in response to air and water temperature increases at the surface [3–6]. However, the environmental impact of geologic emissions [7–9] of subterranean gases has not been well recognized despite the abundance of naturogenic gases stored in sedimentary basins around the globe [10–12]. Yet the triggering mechanism of geologic emissions of naturogenic gases has been poorly understood and remains ambiguous.

Academic Editor: Massimo Zecchin

Received: 9 October 2026
Revised: 16 November 2026
Accepted: 20 November 2026
Published: 26 November 2026

Copyright: © 2026 by the author. Licensee MDPI, Basel, Switzerland. This article is an open access article distributed under the terms and conditions of the Creative Commons Attribution (CC BY) license.

Although it is challenging to partition the absolute magnitude of geologic emissions relative to human-caused emissions, geologic emissions should be considered as input to assess, model, and forecast environmental changes. The objective of this study is to investigate geologic emissions and the underlying causal mechanism.

Among various environmentally harmful gases, methane (CH_4) and radon (R_n) are two mysterious ones that are invisible but pose an immediate threat to the environment. Methane has 28 to 80 times the greenhouse effect of carbon dioxide (CO_2) at decadal timescales [3,7], which contributes to climate changes. Radon [13–19] is radioactive but unnoticeable, which could cause health problems. At the surface, both methane and radon commonly occur in running rivers, hot springs, and soil [4–6]. Wherever emissions intensify to a certain level of concentration at the surface, the flammability of methane and the radioactivity of radon would increase the risk of the contamination of air, soil, and ground water. A focused release of methane and radon, as evidenced by numerous reports from coal mining companies and environmental agencies, could reach a detrimental level of concentration that causes environmental, safety, and health disasters. At the near-surface conditions, methane and radon have been commonly locked and long lived [20–23] but could be easily released to the surface and into the atmosphere. In subsurface conditions, methane and radon are a dominant (70–98%) component of natural gas that is abundant in sedimentary basins, particularly in organic-rich coalbed and shale gas basins that are globally widespread [15].

The methane–radon relationship has been independently established. Grossi et al. [16] reported a first estimation of methane fluxes using the radon tracer method (RTM). Emissions of methane have been estimated experimentally using radioactive radon as an auxiliary tracer, with an established linear relationship between radon and methane concentrations [16]. Mitchell et al. [17] measured radon concentration and natural gas production and reported a positive correlation between methane production and radon concentration [17]. Tait et al. [18] used radon and carbon dioxide concentrations to gain insight into fugitive emissions in a coalbed methane field. They hypothesized that radon may be useful in monitoring methane fluxes from subsurface formations due to changes in geological structures [18]. Wysocka [19] introduced "the radon indicator" of methane outbursts for the hazard prediction.

Unfortunately, geologic emissions and environmental impacts of naturally occurring methane and radon in the subsurface formations [7] have not been extensively and actively monitored, nor have they been routinely used as input in environmental assessment models. Yet the triggering mechanism of geologic emissions of methane and radon has not been well documented. Over the past decades, I have worked on energy exploration projects covering approximately 30 gas basins worldwide. In this study, I revisited the global database of sedimentary basins overprinted by basin-scale wrench, reverse, and normal faults. I also performed dynamic monitoring of radon emissions along wrench, reverse, and normal faults. Based on observational evidence, I proposed a hypothetical interpretation alongside a conceptual model of wrench faults as most efficient pathways for geologic emissions of methane and radon. I argue that my hypothetical model might be applicable to subsurface energy systems in which wrench faults could play a critical role in retaining and enriching energy resources. Facing the double challenges of environmental integrity and energy security, investigating wrench faults should have broad implications for both environmental protection and energy extraction.

2. Materials and Methods

I investigated basin-scale wrench, reverse, and normal faults and their correlations to methane and radon emissions on regional and global scales at the surface and in the subsurface. For methane, I accessed data of both conventional and unconventional gas

basins worldwide from the energy industry, online databases, and other public or private sources. From among the global gas basins, I highlighted the major ones that are overprinted by basin-scale wrench, reverse, and normal faults. I particularly focused on those basins in which major gas fields have been discovered in the industrialized and populated regions, let alone those remote underdeveloped ones.

To demonstrate the concept of gas emissions related to wrench faults in the subsurface, I chose to showcase gas fields in the Appalachian (USA) and Sichuan (China) Basins, the two major gas basins in the western and eastern hemisphere, respectively. I accessed thousands of square kilometers of multi-channel reflection seismic data alongside production data from hundreds of vertical and horizontal wells completed in gas reservoirs. Using seismic amplitude texture as input in seismic structure learning algorithms, I processed seismic data to enhance the visibility of faults and associated structures. Using well logs in the 3D seismic surveys as training data in seismic facies classification algorithms, I converted regular amplitude volumes into seismic facies classification volumes to identify faults, gas chimneys, and vents. Then, I integrated subsurface seismic images, geophysical logs, pore pressure tests, and gas and water production data with surface maps of gas vents, fracture swarms, and topographic lineaments for interpretations.

In general, many intrinsic (geologic) and extrinsic (engineering) factors, including changes in burial depth, the integrity of local structural traps, and sedimentary facies, could affect gas productivity. By using unconventional shale gas fields as test cases, I appropriately deconstructed the primary and secondary relationship between structural and sedimentary gas controls. I selected gas fields that have limited depositional facies variability across the shale reservoirs, narrowing down the attributions of gas productivity primarily to fault/fracture facies, reservoir thickness, and burial depth. I further restricted the comparison to reservoir formations with minimum thickness and depth variations, leaving fault/fracture facies the primary factor for gas productivity.

To monitor real-time emissions of radon gas at the surface, I collected radon seepage data across wrench, reverse, and normal faults in a highly developed and densely populated regime near the coastal city of Shanghai (China). The dynamic emission tests were conducted along an active wrench fault where a moderate magnitude earthquake occurred. Repeated radon measurements were made before and after the earthquake.

I planned survey lines in areas where faults are exposed at the surface to mitigate the uncertainties in fault locality, burial depth, and other factors that could affect radon emissions. The survey lines avoided terrain undulation and Quaternary cover thickness change. The sampling locations avoided thick low-permeability silt or groundwater enrichment zones. All the planning was completed based on Quaternary thickness and fault trace maps alongside wells drilled through the sedimentary cover.

Radon with a half-life of 3.8 days could emits α-rays that are much stronger than X-rays. The emitted particles could penetrate mica and nitrogen fibers, causing radiation damage as latent α-tracks. The latent α-tracks became permanent ones after chemical etching. Under a microscope (10 × 40), the α-tracks were counted in a unit area (N mm^{-2}) as an estimate of the concentration of radon. The original data were quality checked to minimize possible errors. The baseline (normal) α-track intensity was estimated using background measurements in the region outside of the fault zone. Two times standard deviation plus the baseline value ($b + 2\sigma$) was regarded as being abnormal concentration of radon.

Following subsurface remote sensing and surface direct measurements, I proposed a hypothetical interpretation alongside conceptual models to explain the observational and monitoring results. There are numerous variables that could affect gas flows along faults in the subsurface, which include but are not limited to gas volume, pressure, temperature, dynamic viscosity, phase changes, and relative permeability during multiphase fluid flow

in porous media. To focus on the fault dip and its control to gas flows, I reduced the number of variables and held all the other uncertain variables constant for comparative analysis of wrench faults with respect to reverse and normal faults. The purpose of the conceptual modeling was to characterize and differentiate the impact of wrench faults on gas emissions relative to reverse and normal faults. For that purpose, I designed a first-order modeling scheme that locks all the variables except fault dip, gas buoyancy, and fault resistance that are relevant to the differentiation of wrench faults from reverse and normal faults. Such a reduced-order modeling method was used to assess the impact of individual variables that are of most relevance and interest among all the other variables of gas emission systems.

3. Results

3.1. Subsurface Remote Sensing

Geologic leakage and venting of subsurface methane have been commonly observed worldwide [24–30], and their relations to wrench faults have been previously reported [10,31,32]. Figure 1, which only represents part of the global gas basins in the database, highlights major gas basins on present-day and paleo continental margins that were overprinted by basin-scale wrench, reverse, and normal faults. As indicated in the base map, there are numerous gas basins in highly industrialized and densely populated regions around the globe. The basins contain both conventional natural gas and unconventional shale gas. These gas basins were developed early by conventional drilling and later by unconventional hydraulic fracturing. Dynamic interactions between wrench faults and natural gas alongside hydrothermal fluids have been reflected both at the surface and in the subsurface (Figure 1). At the surface, gas vents, mud volcanoes, pockmarks, and gas chimneys along with hydrothermal fluids were commonplace and spatiotemporally associated with wrench faults. Terrestrial and marine seepages have been active along wrench faults for a long geological time and are widespread all over the world [7,9,24]. In the subsurface, the wrench faults penetrated gas-saturated reservoirs in conventional and unconventional gas basins, both onshore and offshore (Figures 1–3). They occurred in rift and foreland basins as transfer or tear faults to connect gas sources in the subsurface with gas vents at the surface. Upward migrations of vast volumes of thermogenic methane were evidenced by numerous discoveries of gas fields associated with wrench faults. Measurements of gas flow rates and formation pressures indicated that dissociated natural gas has been migrating upwards, leaving behind pressure sinks with depleted gas along the wrench faults that were invaded by salt diapirs and hydrothermal fluids (Figures 1 and 2).

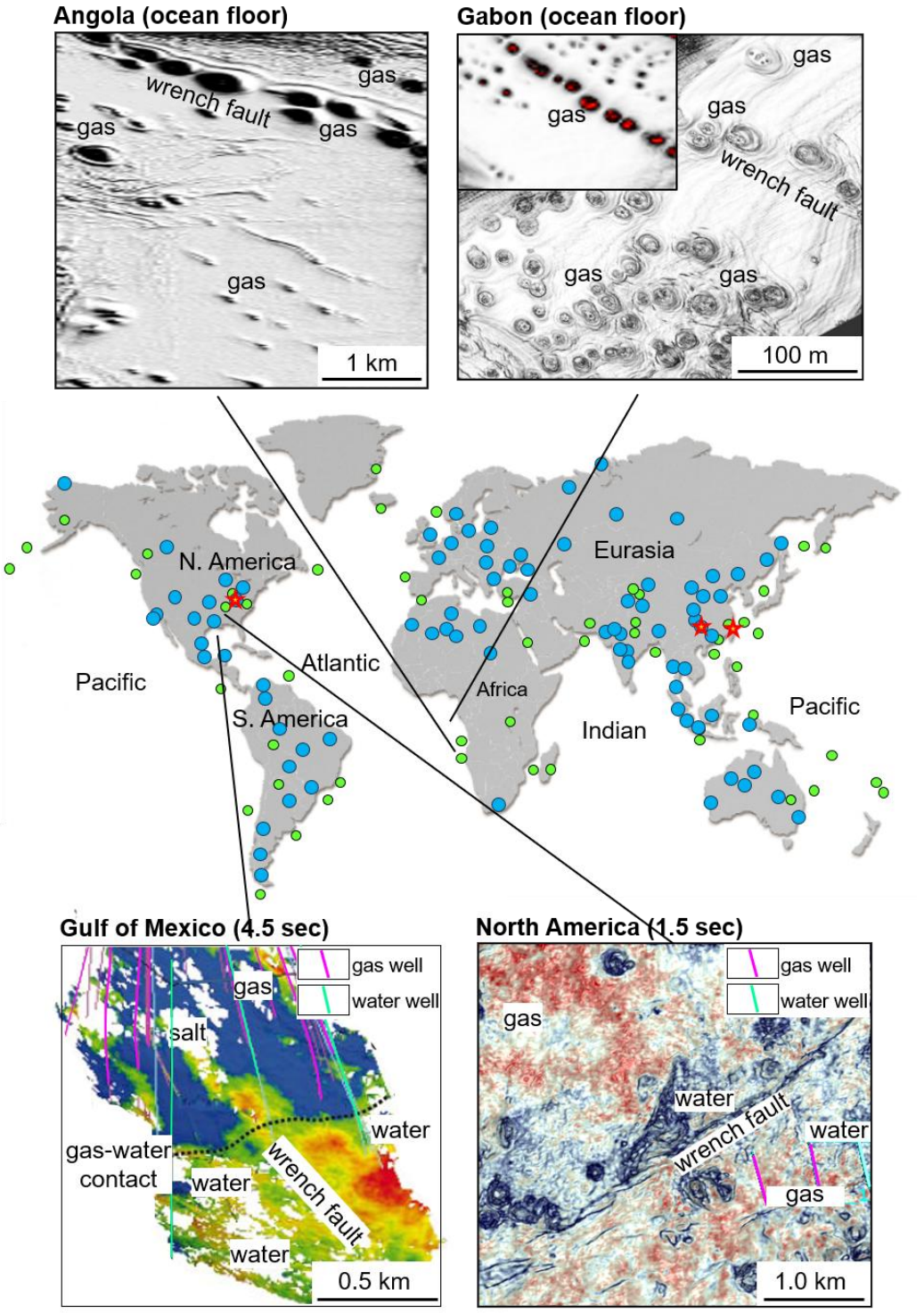


Figure 1. Location index map of major gas basins that have been well developed and overprinted by basin-scale wrench, normal, and reverse faults (data sources are from energy companies, online data base [11], U.S. Energy Information Administration Advanced Resources International Inc. [12], and published and unpublished reports). Green and blue dots highlight conventional and unconventional gas basins [10–12], respectively. Red stars are the locations of methane and radon gas fields showcased in this study. Major gas basins are highly condensed for the illustrative purpose of the extensiveness of potential gas leaks. Only a portion of gas basins are selected from the database based on potential gas reserves with possible geographic biases between well-developed and underdeveloped regions (basins). Example images are selected from the database to

highlight surface gas vents and pockmarks (top) alongside subsurface gas gaps and hydrothermal fluids (bottom) along wrench faults, although normal and reverse faults should also have contributed to gas emissions.

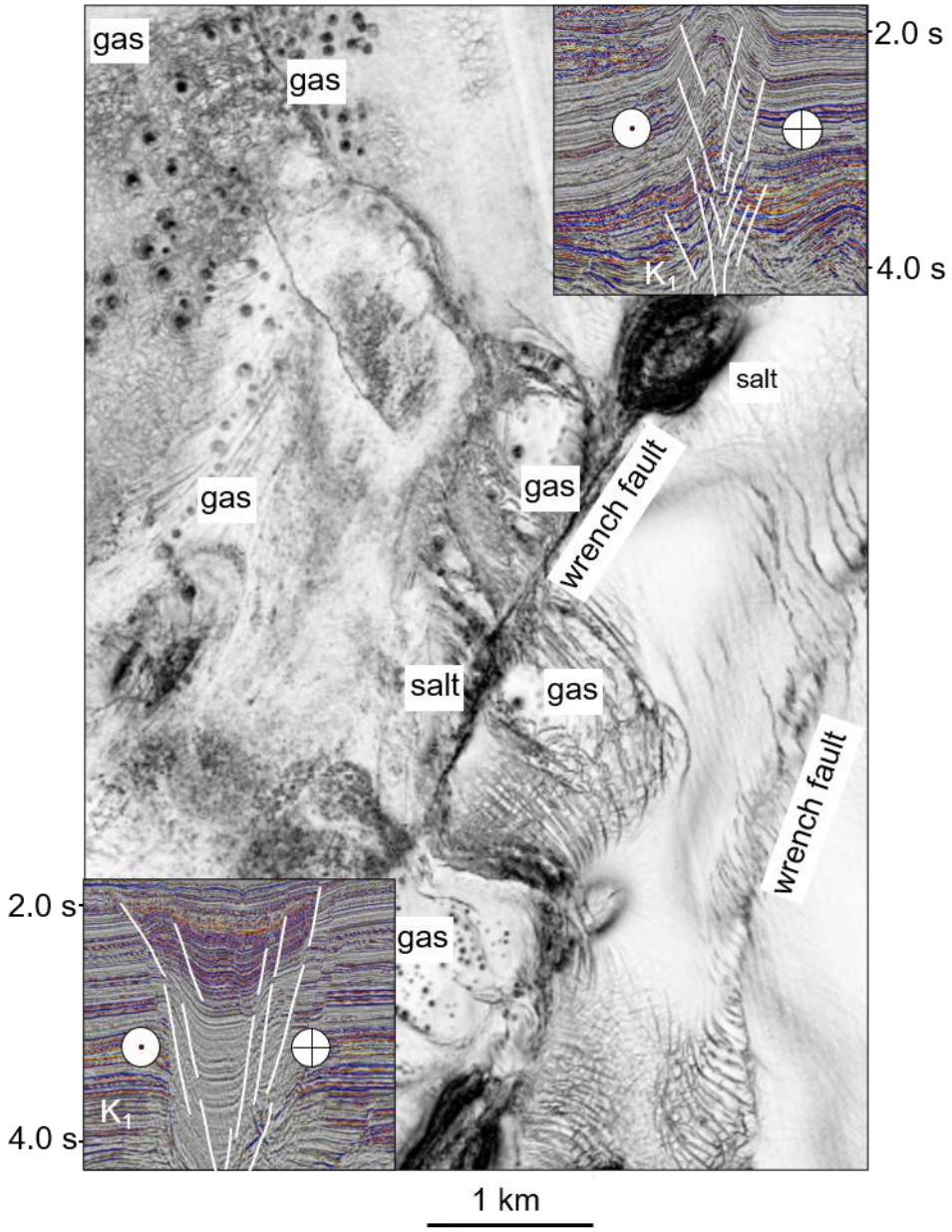


Figure 2. Example images selected from the database showing gas vents related to wrench faults. The map (black and white) is a machine-generated image highlighting gas vents, salt diapirs, wrench faults, and associated structures. The vertical seismic sections (color) show transpression and transtension related to wrench faulting. The en-echelon faults and fractures in the map view, alongside negative and positive flower structures in the cross-sectional views, are kinematically indicative of the left-lateral sense of shear and geometrically indicative of the steep dips of the wrench faults.

Among the well-known gas fields that were reported to be related to wrench faults are those in the Appalachian and Sichuan Basins, the two representative gas basins in the western and eastern hemisphere, respectively. The gas fields in the Appalachian and Sichuan Basins sit underneath densely populated regions. Historically, both gas basins witnessed the earliest discoveries of natural gas. Geologically, both gas basins experienced rift (normal) faulting on passive margins and were overprinted by reverse and wrench

faulting in foreland basins. Furthermore, both basins generated and contained huge volumes of methane with a long successful history of exploration for and production of conventional natural gas and unconventional shale gas.

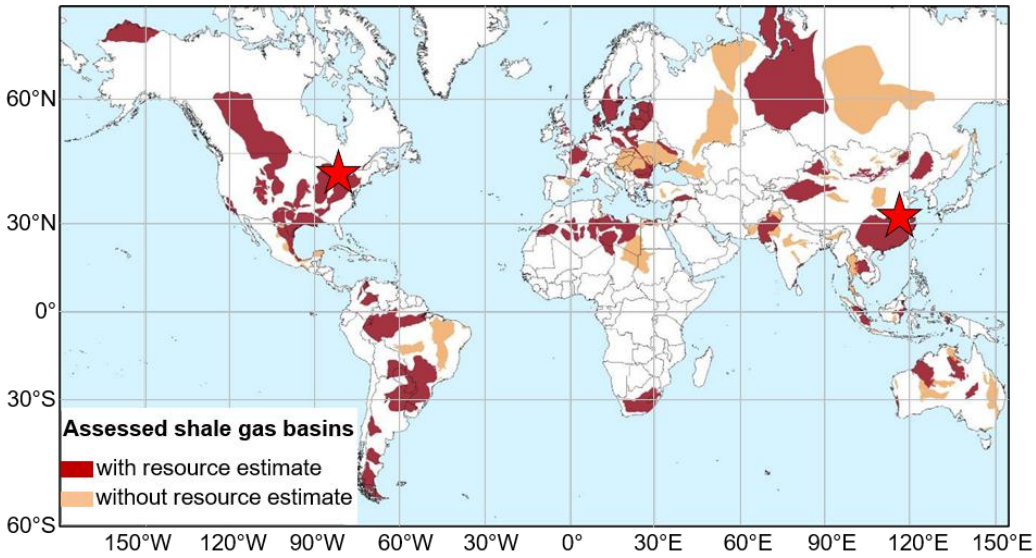


Figure 3. Major shale gas basins (data source is from U.S. Energy Information Administration based on Advanced Resources International Inc. [12]). Only a portion of gas basins are highlighted from the database. The two red stars are the gas fields in the Appalachian and Sichuan Basins showcased in this study.

3.1.1. Case Study in the Appalachian Basin

The Appalachian Basin witnessed the earliest discoveries of gas venting in North America related to wrench faults that are deeply rooted in the Paleozoic reservoir formations [31,33]. The Paleozoic rift and foreland basins were overprinted by cross-regional northwest-trending wrench faults [33–38], as transfer or tear faults crosscutting organic-rich shales and gas-saturated sands (Figure 4). In the early 1800s, on finding the first gas vent, the first gas well was drilled to a depth of 21 meters near the active gas vent in the northern Appalachian Basin. In the same time frame, natural gas alongside salt was also found at the surface and in shallow exploratory wells in the central Appalachian Basin. The escaping gas was observed causing burning creeks and burning springs. The exploratory well bores struck large amounts of gas along with salt water at shallow depths of less than 305 meters. Apparently, the upwellings of buoyant gas and low-density salt alongside hydrothermal waters have been related to wrench faults [38]. Since then, more gas vents, burning waters, and burning rocks have been reported where wrench faults dominate [36] (Figure 5). In the most recent two decades, large volumes of unconventional gas have been extracted from the organic-rich Marcellus shale of the Middle Devonian at depths of 610–2743 meters [39–41] (Figure 5). Well tests showed that gas pressure drops significantly towards the wrench faults [31] (Figure 5). Historic gas production data demonstrate an overall decline in gas flow rates towards the wrench faults [31] (Figure 5). Fault/fracture and facies classifications based on seismic amplitude using unsupervised machine learning algorithms are expressive of enhanced fracture intensity along with gas seepages and salt flows towards the wrench faults [31]. At the surface, the wrench faults crop out as fracture swarms [42]. An overwhelming majority of rivers are consistently running in a preferred northwesterly orientation, which are parallel to the northwest-trending wrench faults directly observed at the surface [42] and remotely imaged in the

subsurface [31]. Throughout the Appalachian Basin, the wrench faults are commonplace and were successfully used as an exploration tool for natural gas [35].

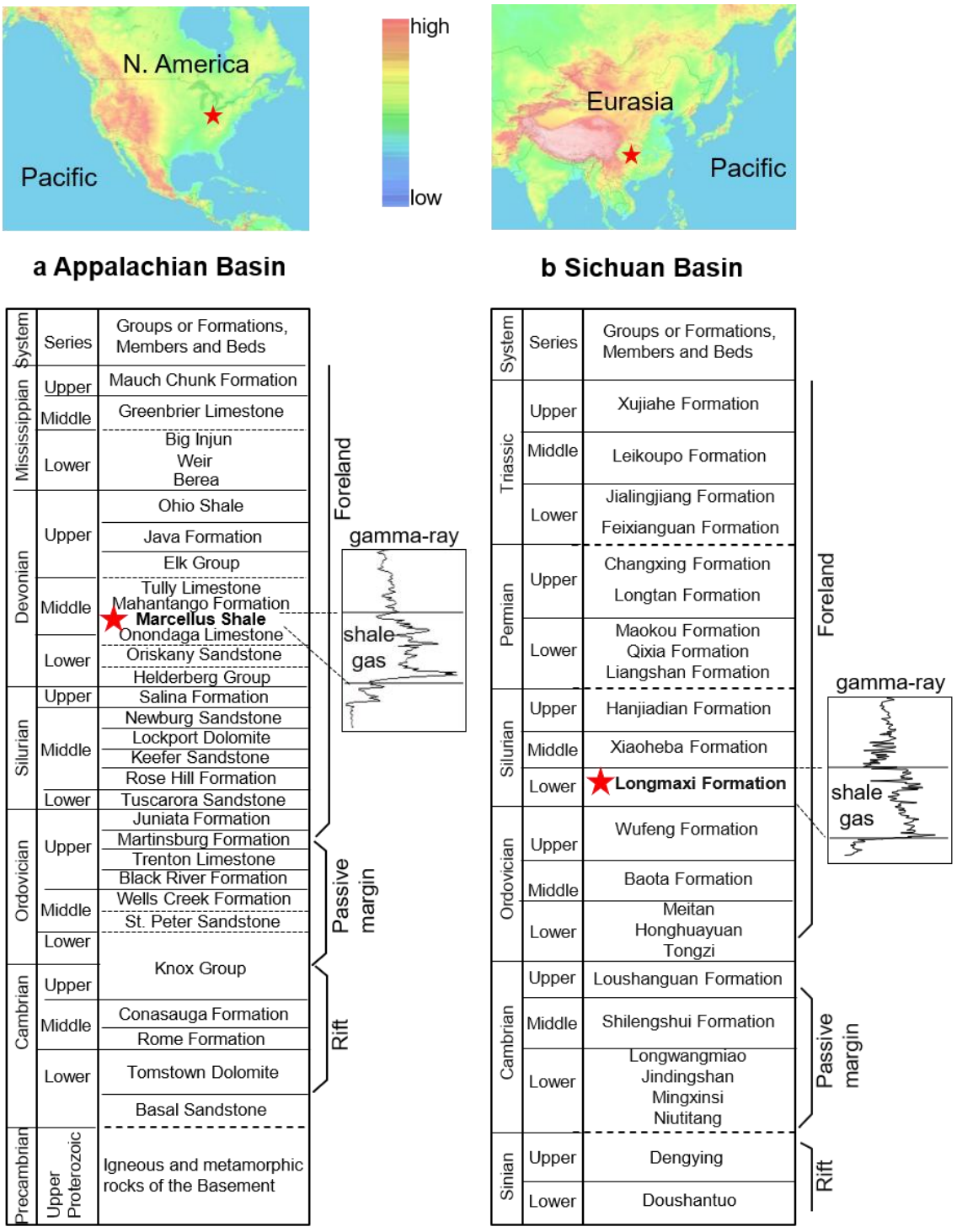


Figure 4. Stratigraphic nomenclature in the Appalachian and Sichuan Basins with the main shale gas reservoirs being highlighted. The well logs show gamma ray anomalies of the organic-rich formations. Red stars are the source rocks of the gas fields showcased in this study. (**a**) Middle Devonian Marcellus shale in the Appalachian Basin. (**b**) Lower Silurian Longmaxi shale in the Sichuan Basin.

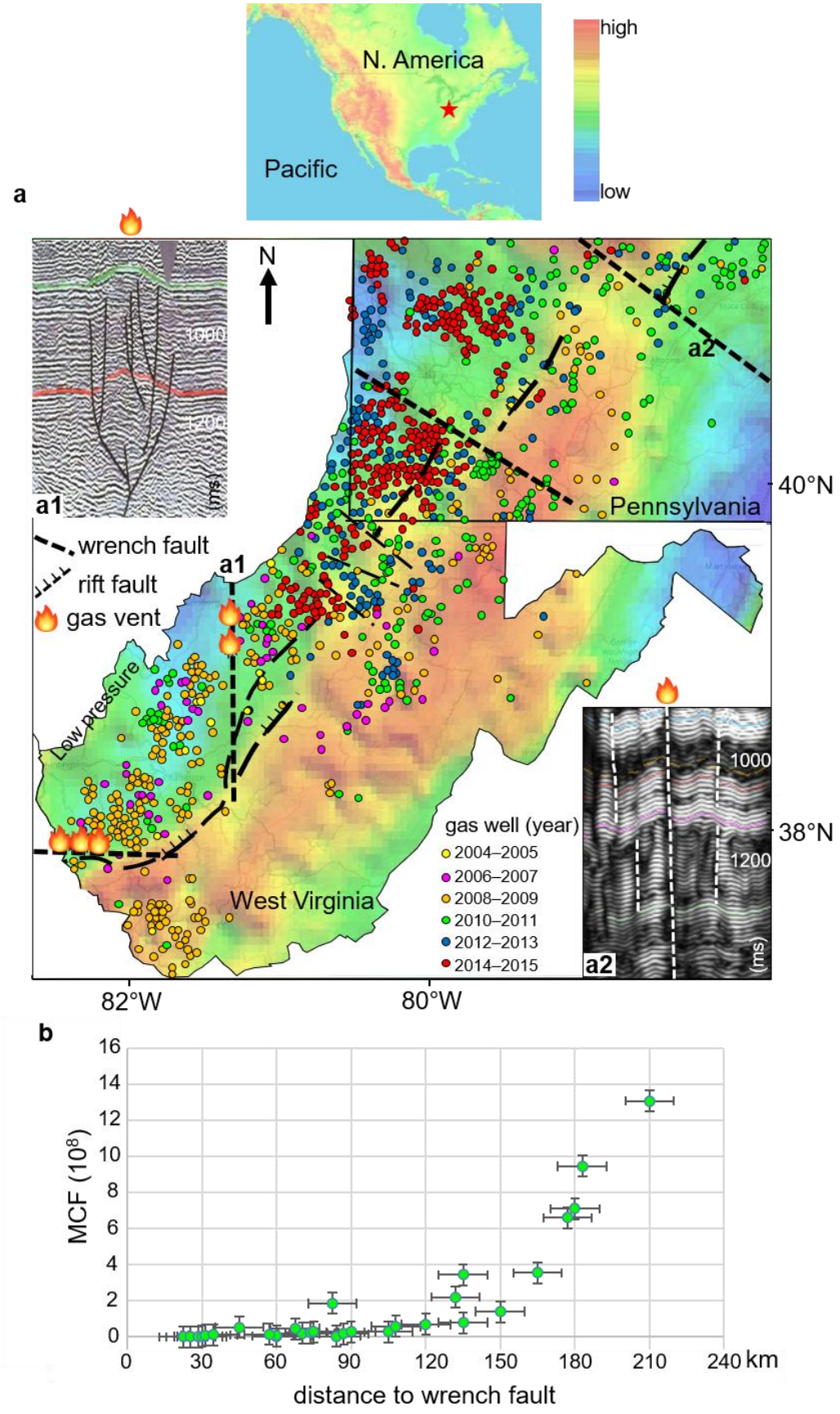


Figure 5. Surface gas vents and subsurface shale gas operations in relation to the wrench faults in central Appalachian Basin (USA) [31]. The red star is the location of the gas field. (**a**) Shale gas wells completed from 2004 to 2015 (http://marcellus.psu.edu) (accessed on 1 January 2018) overlaid with major wrench and rift faults in the north central Appalachian Basin. The background color shows

gravity intensity, with warm color denoting gravity high and cold color gravity low (https://cellcode.us/quotes/states-map-united-gravity.html) (accessed on 1 January 2018). The inserts are seismic sections showing wrench faults [36,37]. (**b**) Average yearly gas flow rate related to the distance to the wrench fault in the state of Pennsylvania. The green dots with error bars are historical (2017) gas flow rates of thirty counties across the state [31].

3D seismic imagery (Figure 6) demonstrates that wrench faults dominate over reverse faults in controlling gas and salt flows, which is reflected by the differences in seismic patterns between the wrench and reverse faults. (1) In the wrench fault section, vertically diffusive zones of homogeneous amplitude texture are suggestive of gas saturation with low impedance contrast. In contrast, in the reverse fault section, such amplitude texture is lacking. (2) The top salt surface map shows northwest-trending ridges that are correlated to the wrench faults but not to the reverse and normal faults. In the wrench fault section, salt domes are indicative of salt flows controlled by the wrench faults. In contrast, in the reverse fault section, the salt domal features are lacking along reverse and normal faults, whereas the flat salt top is indicative of little control of the reverse faults on salt flows. (3) The wrench faults with steep dips consistently cut deep through all the reservoir formations. In contrast, the reverse and normal faults with shallow dips cut through a limited depth window.

3.1.2. Case Study in the Sichuan Basin

The Sichuan Basin witnessed the earliest discoveries of gas venting in eastern Asia related to wrench faults that are deeply rooted in the Paleozoic reservoir formations [32,43]. Dating back to 211 BCE, the first natural gas alongside salt was found in a well at a depth of 150 meters in the central Sichuan Basin [43]. In the early 1800s, in the eastern Sichuan Basin, shallow gas was found to be sourced in an intensely faulted reservoir of the Upper Triassic at a depth of 1000 meters [43]. The Sichuan Basin experienced a successful gas exploration history associated with wrench faults and replicated the correlation of wrench faults to natural gas enrichment. The pre-Cambrian rift basin and the late Paleozoic foreland basin were overprinted by cross-regional northwest-trending wrench faults [44] as transfer or tear faults crosscutting organic-rich shales and gas-saturated sands (Figure 4). Over the past decades, the Sichuan Basin has witnessed extensive shale gas development. The first and the largest shale gas field was discovered in the Longmaxi shale of the Lower Silurian at depths of 2000–4000 meters [45–49]. The gas field is bound to the south by a major wrench fault [47]. Feeding back to the enhanced fracture intensity and permeability along the wrench fault, both pore pressures and gas flow rates drop significantly within the wrench fault zone (Figure 7). Based on cumulative gas flows (Mmcf) and normalized flow rates (Mmcf day^{-1}), the top 50% productive wells were drilled in the distal areas clear of the wrench fault, yielding the highest volume of gas but the lowest volume of water. In contrast, the bottom 50% non-productive wells were drilled near the wrench fault, yielding the lowest volume of gas but the highest volume of water [46,47] (Figure 7). Borehole microseismic monitoring indicated that all the microseismic events were triggered by steeply dipping (>60°) fractures. An overwhelming majority of microseismic events were related to fractures with a dipping angle of 70°–90° and a strike-slip focal mechanism [50], which is consistent with regional observations of dominant strike-slip focal mechanisms of small earthquakes in the basin [51,52]. Unlike the northwest-trending wrench faults, the two reverse faults show little or moderate correlation to pore pressures. The pore pressures across the two northeast-trending reverse faults were less perturbated than those across the northwest-trending wrench faults. Likewise, the gas productivity was much higher whereas the water productivity was much lower in the reverse faults than in the wrench faults.

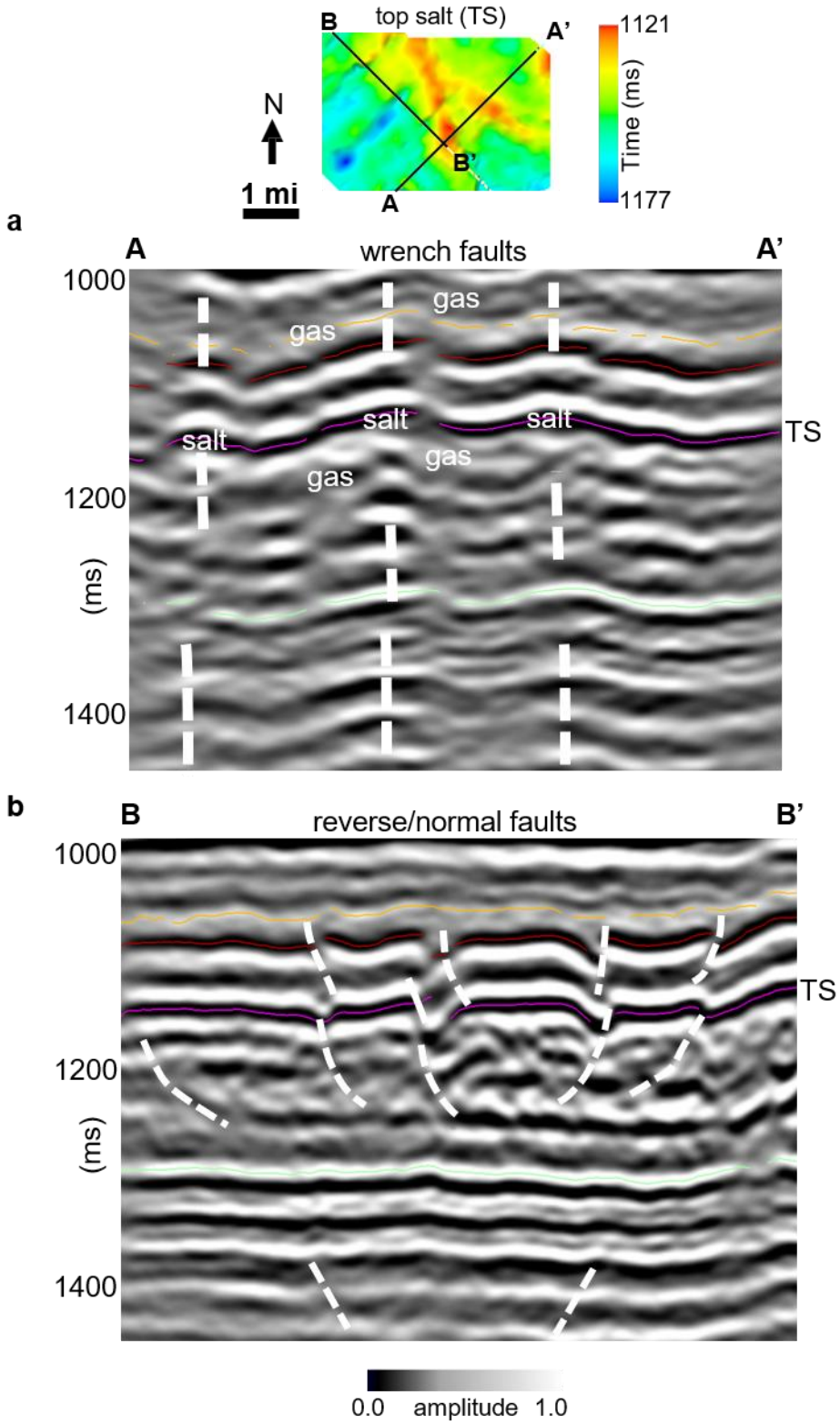


Figure 6. Reflection seismic patterns of wrench faults compared with those of reverse/normal faults [31]. (**a**) Wrench faults are vertical and associated with gas chimneys and salt domes. Gas flows are expressed by the vertical zones of low amplitude homogeneous texture aligned with the wrench faults. Salt flows are indicated by the salt ridges aligned along the wrench faults. (**b**) Reverse/normal faults are dipping and free of gas chimneys and salt domes.

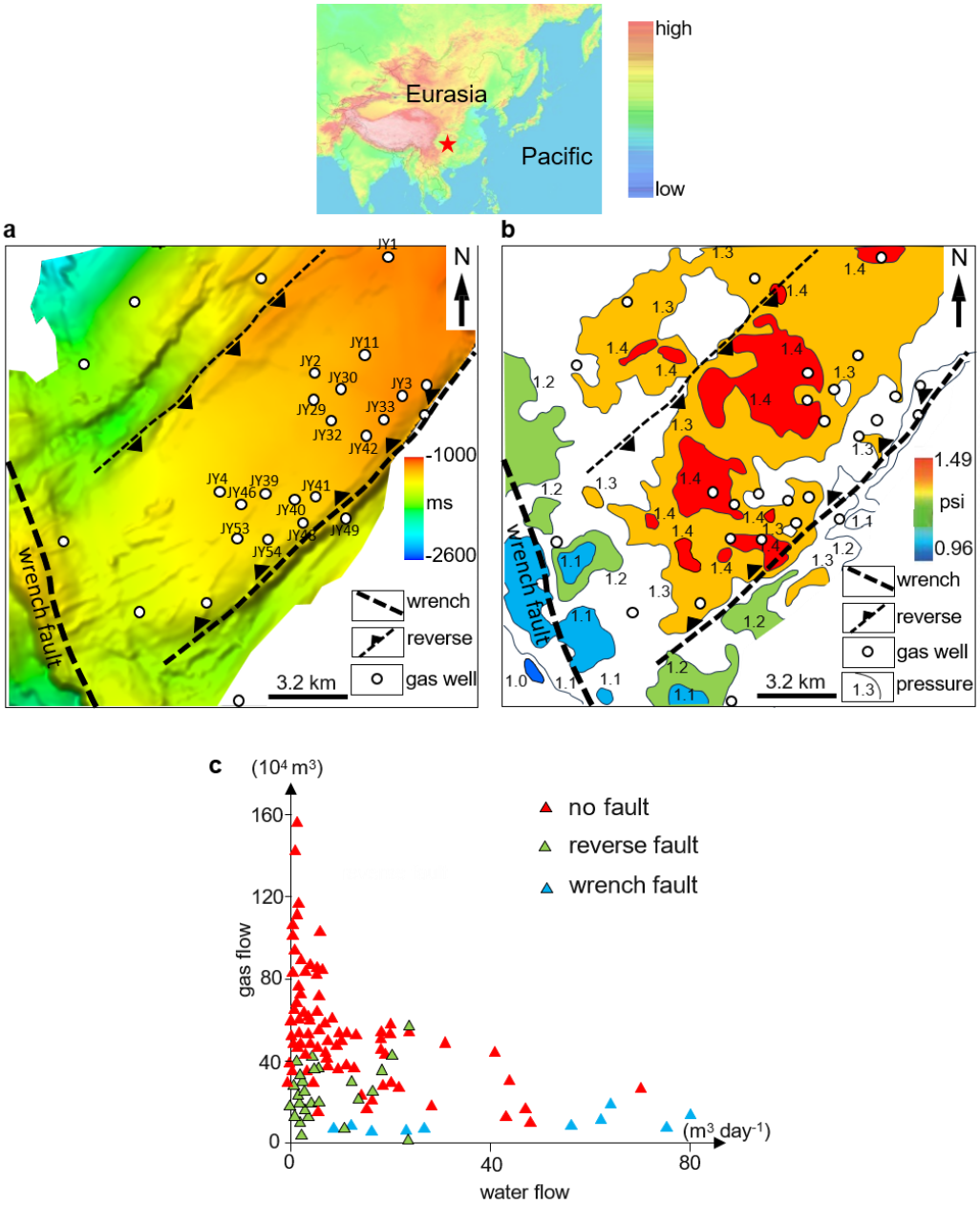


Figure 7. Subsurface gas pressures and flow rates of a gas field in the Sichuan Basin (China) [32]. The red star is the location of the gas field. (**a**) Time structures of the top Longmaxi shale overlaid with the wrench and reverse faults. (**b**) Pore pressures [32,47] overlaid with the wrench and reverse faults. Pore pressure drops substantially to the lowest level near the wrench fault but reaches to the highest level distant from the wrench fault. (**c**) Shale gas flow rates vs. water flow rates of wells [32,47]. The wrench fault is associated with the lowest gas flow rate but the highest water flow rate.

3D seismic imagery (Figure 8) demonstrates that the wrench faults dominate over the reverse faults in controlling gas and water flows, which is reflected by the differences in seismic reflection patterns between the wrench and reverse faults. (1) In the map view of a reservoir formation, facies classification changes dramatically from the north toward the wrench fault in the south. The northwest-trending wrench fault is associated with a zone of distinct fault/fracture facies, which crosscut depositional facies. In contrast, the two northeast-trending reverse faults show little or moderate facies variations without an apparent cross-cutting relationship to depositional facies. (2) The wrench faults are steep, deep, wide, and destructed all reservoir formations. In contrast, the reverse and normal faults are dipping, shallow, narrow, and cut through limited sequences of reservoir formations.

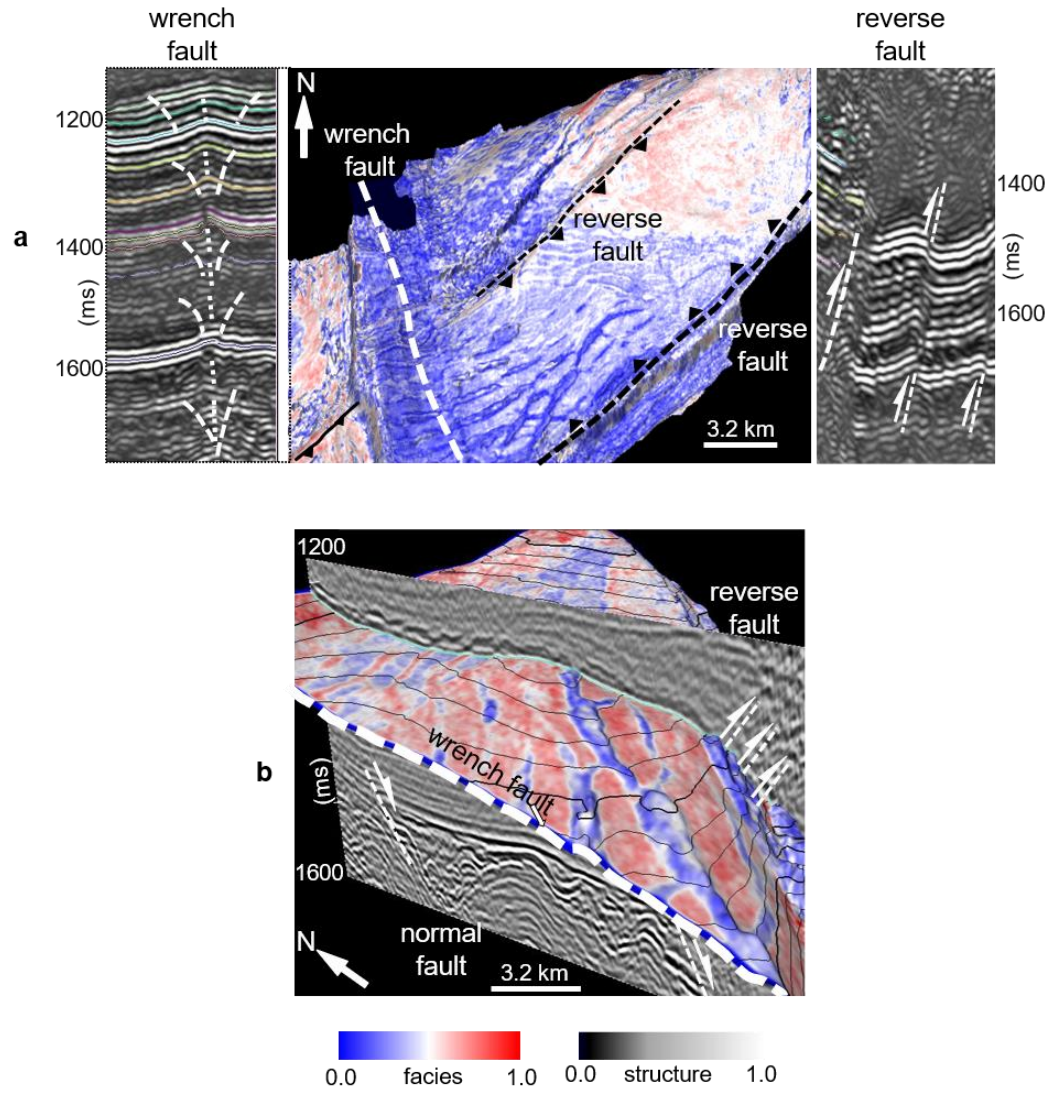


Figure 8. Reflection seismic patterns of wrench faults compared with those of reverse/normal faults [32]. (**a**) Seismic facies map of the Longmaxi shale (color) alongside cross sections of wrench and reverse faults (black and white). Wrench fault zone features a distinctive fracture facies (blue) that crosscuts reservoir depositional facies (red). Reverse/normal faults show no distinct fracture facies and cross-cutting relationship to depositional facies. (**b**) Horizon slice of reservoir depositional facies (color) draped over reservoir structures (think black contour lines) of the Longmaxi shale cross cut by the wrench fault (thick dashed white line), co-displayed with a vertical seismic section (gray) of reverse and normal faults (thin dashed white lines alongside arrows).

3.2. Surface Monitoring

A large-scale active (seismogenic) wrench fault system in the suburban areas of the coastal city of Shanghai (China), near the coastline of the East China Sea [53], offered an opportunity to measure and monitor gas emissions along active wrench faults. A magnitude 5.1 earthquake occurred on one of the wrench faults. Repeated monitoring of radon gas before and after the earthquake, using α-tracks left by the α-rays emitted from radon, resulted in both static and dynamic measurement data for comparative analysis.

Pre-quake measurements showed that radon concentrations on the wrench faults were significantly higher than the background off the faults (Figure 9). Comparisons among all the survey lines demonstrated that the wrench faults distinguished themselves from the normal and reverse faults in radon concentration. Among all the lines, lines 6 and 7 traversing the reverse and normal faults in the eastern survey area showed the lowest level

of radon emissions. Both the northern and southern wrench faults witnessed relatively higher emission intensity than the eastern region where reverse and normal faults dominate. Although there were only nine survey lines in the survey region, the overall pattern was suggestive if not indicative of the distinction between the two conjugate wrench fault zones and reverse/normal faults in terms of emission efficiency of radon.

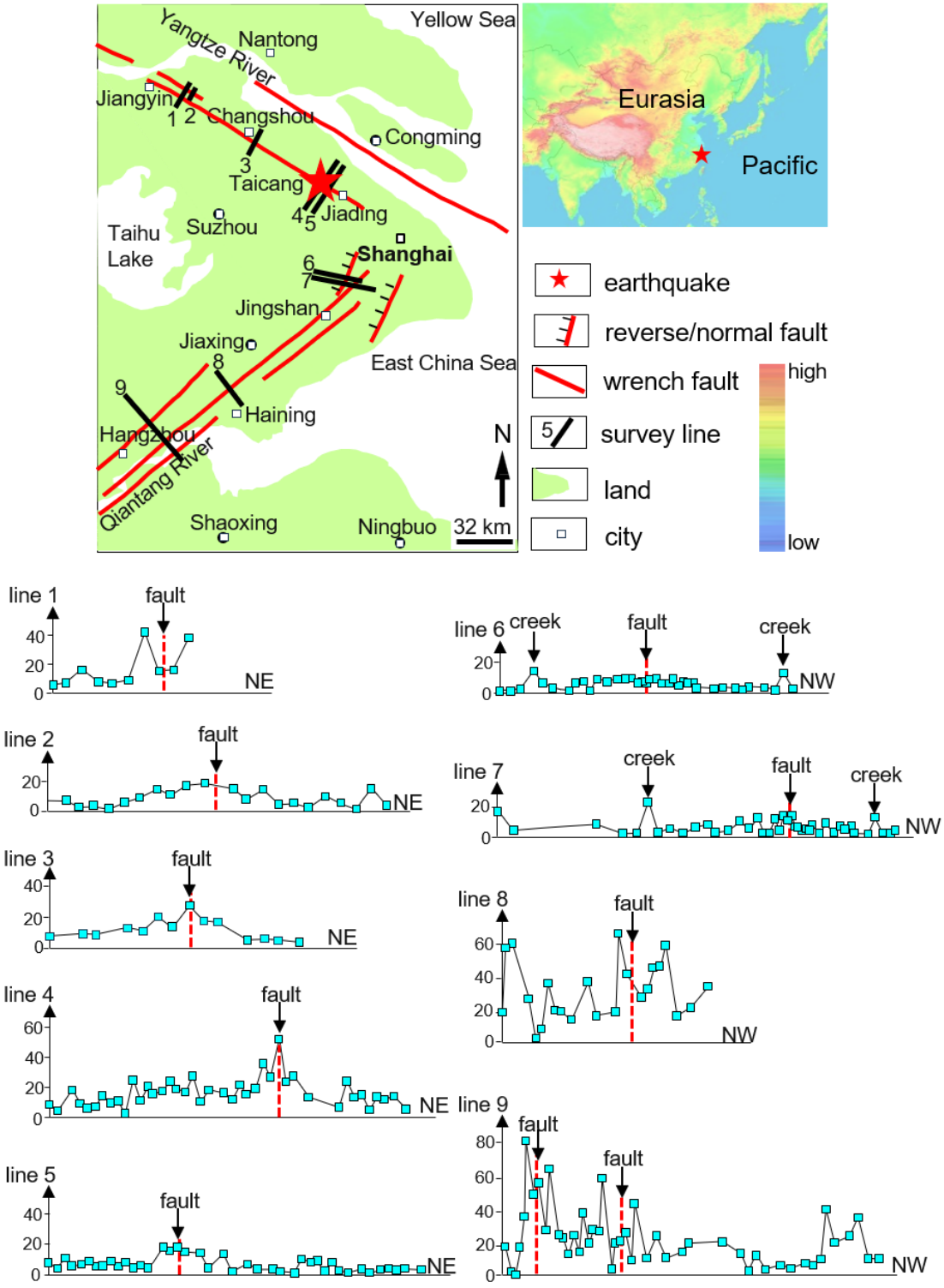


Figure 9. Baseline surveys of radon gas emissions along wrench and reverse/normal faults in the suburban area of the coastal city Shanghai (China) near the East China Sea [53]. Survey lines 1–5 cross the southeast-trending wrench fault zone. Survey lines 8 and 9 cross the northeast-trending wrench fault zone. Survey lines 6 and 7 cross a north-northeast-trending reverse/normal fault.

Following the pre-quake measurements, repeated measurements demonstrate dynamic emissions of the active wrench fault in the north where the earthquake occurred. Post-quake measurements indicated that the gas flux was 2–3 times higher than before the earthquake (Figure 10). The time lag monitoring results warned that the youngest wrench faults, particularly the most recently active ones, could trigger radon to flood to the surface in a short (daily or hourly) time frame.

Radon is released from the decay chains of uranium that is 10–100 times more concentrated in the organic-rich formations in the subsurface than the global average [13] (Figure 4). Previously conducted radon surveys in gas basins indicated that abnormal radon fluxes at the surface reflect fractures and hydrocarbon leaks in the subsurface [14,15]. Radon anomalies were found to be directly correlated with the proximity to the uranium-rich shales and indirectly correlated with topographic lineaments and bedrock fractures [14]. Laboratory experimental data of soil samples compared with field α-track data apparently point towards the origin of radon in the subsurface formations [14], suggesting long-distance upwards migrations of radon from subterranean organic-rich materials.

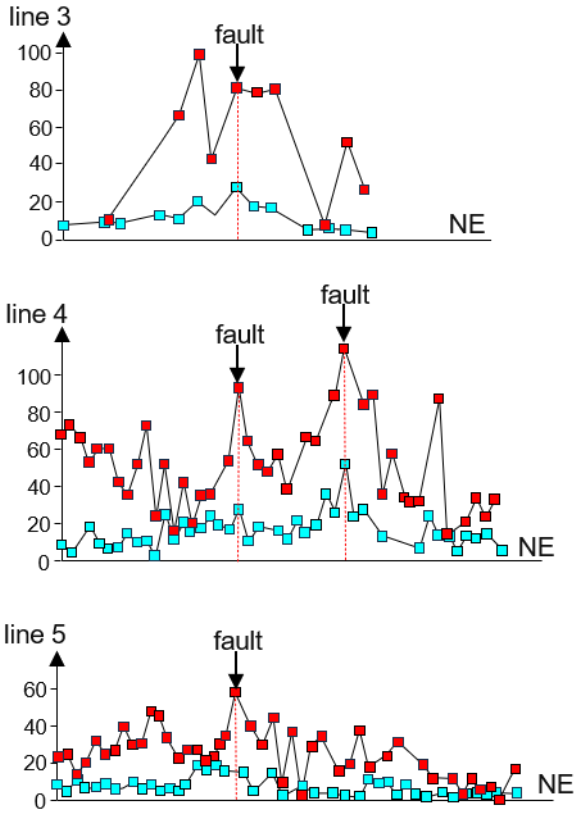


Figure 10. Monitoring surveys of radon gas emissions across the seismogenic wrench fault before and after a magnitude 5.1 earthquake in the suburban areas of the coastal city Shanghai (China) [53]. The three survey lines are close to the epicenter of the earthquake, and the post-quake radon concentrations (red) are 2–3 times the pre-quake ones (blue). Locations of survey lines are shown in Figure 9.

4. Discussion

4.1. Hypothetic Interpretations

The unique orientation of wrench faults relative to buoyancy and lithostatic stress makes wrench faults distinctive from reverse and normal faults in terms of the efficiency of gas emissions and the potential of shear failures. The maximum partitioning of gas buoyancy parallel to wrench faults, coupled with the minimum partitioning of gas buoyancy normal to wrench faults, warrants the maximum driving power for upward gas

flows. Vertical lithostatic stress might impose the least compaction of wrench faults, and vertical intermediate principal stress ($\sigma_2 = \rho_{lith}z$) could impose maximum shear along vertically conjugate fractures, which could enhance the vertical connectivity of fracture networks and promote gas emissions.

Figure 11 is a conceptual model from a geometrical perspective demonstrating the gas emission potential of wrench faults compared with that of reverse and normal faults. The model assumes that gas emissions are driven by the buoyancy of gas against the drag of faults, both of which rely on the partitioning of the vertical buoyant force into two components, one being parallel (shear) and the other perpendicular (normal) to the faults. By holding all the other unknown contributing variables locked, the model highlights the efficiency of gas emissions as a function of gas density, gas buoyancy, fault dip, and gas-fault frictional coefficient as expressed by Equations (1)–(3).

$$z = \frac{f}{2\rho_{gas}} sin\alpha\ (sin\alpha - \mu cos\alpha)t^2 \quad (1)$$

$$v = \frac{f}{\rho_{gas}} sin\alpha\ (sin\alpha - \mu cos\alpha)t \quad (2)$$

$$t = \frac{(2\rho_{gas}z)^{1/2}}{f[sin\alpha\ (sin\alpha - \mu cos\alpha)]^{1/2}} \quad (3)$$

where z denotes the vertical ascent distance (m) from the subsurface source towards surface sink; v is the instantaneous vertical ascending velocity (m s^{-1}); t is the emission time (second) required for the gas to reach the surface; f is unit-volume buoyant force (N m^{-3}); α is fault dip (degree); ρ_{gas} is gas density (kg m^{-3}); and μ is frictional coefficient (dimensionless). Equation (1) is derived from Newton's law of flow, in which $f(sin\alpha - \mu cos\alpha)$ is the net unit-volume buoyant force parallel to fault with the first term being the fault parallel buoyancy and the second term the frictional resistance; Equation (2) is derived by taking the first derivative of Equation (1); Equation (3) is derived by taking the square root of Equation (1). The equations indicate that the dipping angle α of faults dictates the vertical ascent distance z, the instantaneous ascending velocity v, and the time t required for gas to escape from the subsurface source to the surface sink (Figure 11) (Supplementary Data S1–S3). Generally, the efficiency of gas flow is modulated by the dominance of the fault parallel (shear) component over the fault orthogonal (normal) component of buoyancy, which varies with fault dip. As fault dip increases from 0° to 90°, the dominance and gas flow rate increase dramatically, making vertical faults the fastest track pathways for gas emissions. Statistically, wrench faults have characteristic dips of 60°–90° and typically steeper than normal and reverse faults, although steep normal and reverse faults also exist. It then follows that wrench faults typically act as the fastest track pathways for geologic emissions of subsurface gases.

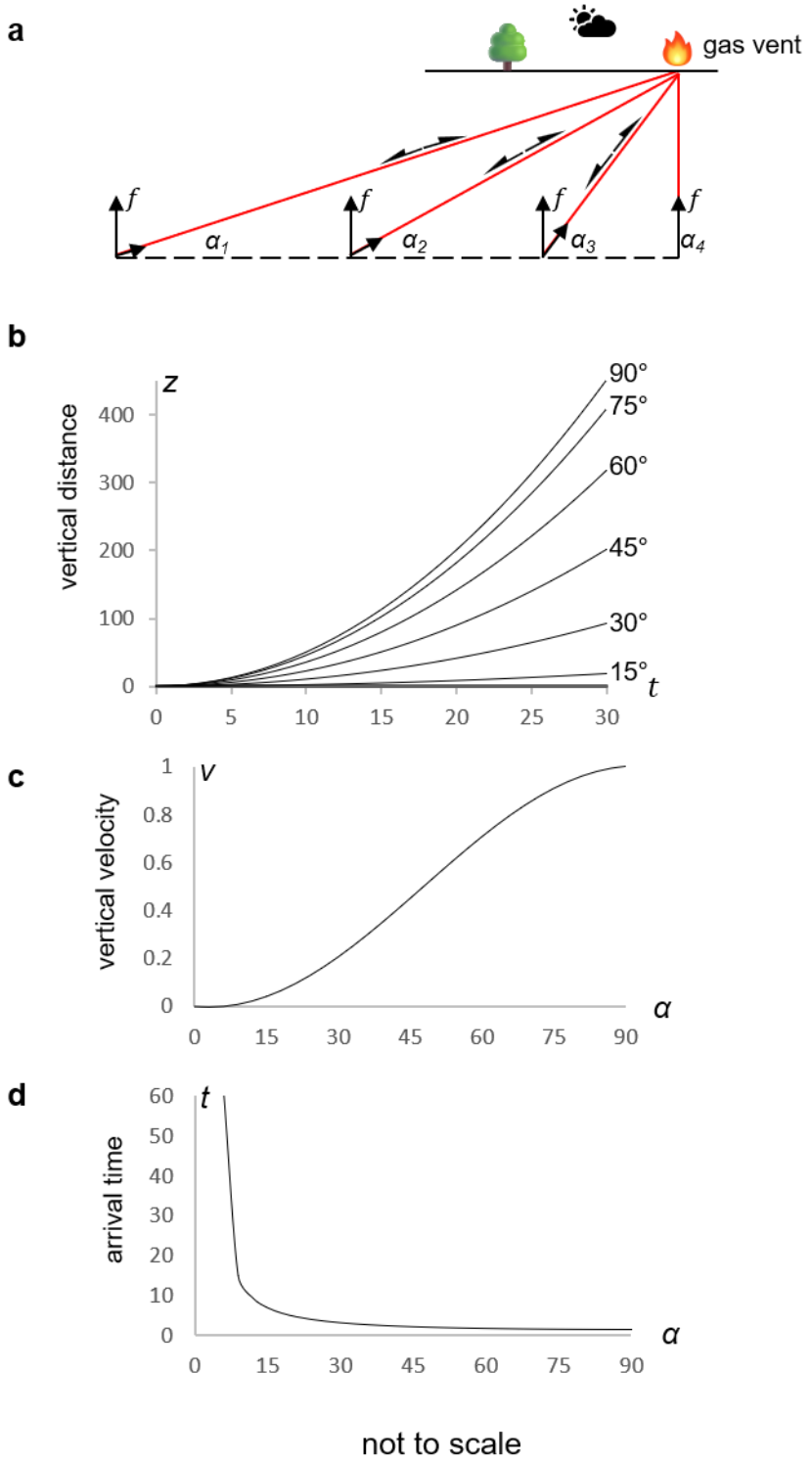


Figure 11. A reduced-order conceptual model showing gas emission efficiency through faults of varying dip (Supplementary Data S1–S3). The flow distance, rate, and time are relative values (not to scale) for comparison only. (**a**) Vertical profile of faults with varying dips α alongside vertical buoyancy f in the subsurface. (**b**) Vertical ascent distance z of gas as a function of time t required to reach the surface and fault dip α. (**c**) Instantaneous ascending velocity v of gas as a function of fault dip α. (**d**) Escape time t required for leaking gas to reach the surface as a function of fault dip α.

Figure 12 is a conceptual model from a geomechanical perspective, demonstrating the shear failure potential of wrench faults compared with that of reverse and normal faults. The model suggests that wrench faults are distinct from reverse and normal faults

in the magnitude of differential stress and the orientation of principal stresses, which control the potential of shear failure of reservoirs and caprocks. Based on Mohr–Coulomb theory, wrench, reverse, and normal faults are here expressed by three Mohr circles in red, green, and blue, respectively (Figure 12). The corresponding stress regimes are represented by Equations (4) and (5) for wrench faults, Equations (6) and (7) for reverse faults, and Equations (8) and (9) for normal faults.

$$\sigma_n = \frac{1}{2}(\sigma_1 + \sigma_3) + \frac{1}{2}(\sigma_1 - \sigma_3)cos2\theta \quad (4)$$

$$\sigma_s = \frac{1}{2}(\sigma_1 - \sigma_3)sin2\theta \quad (5)$$

$$\sigma_n = \frac{1}{2}(\sigma_1 + \rho_{lith}z) + \frac{1}{2}(\sigma_1 - \rho_{lith}z)cos2\theta \quad (6)$$

$$\sigma_s = \frac{1}{2}(\sigma_1 - \rho_{lith}z)sin2\theta \quad (7)$$

$$\sigma_n = \frac{1}{2}(\rho_{lith}z + \sigma_3) + \frac{1}{2}(\rho_{lith}z - \sigma_3)cos2\theta \quad (8)$$

$$\sigma_s = \frac{1}{2}(\rho_{lith}z - \sigma_3)sin2\theta \quad (9)$$

where σ_n is normal stress (N m^{-2}); σ_s is shear stress (N m^{-2}); σ_1 is maximum principal stress (N m^{-2}); σ_3 is minimum principal stress (N m^{-2}); ρ_{lith} is lithostatic density (kg m^{-3}); z is depth (m); and θ is potential fracture orientation (degree) relative to minimum principal stress. Generally, the maximum differential stress related to wrench faults ($\sigma_1 - \sigma_3$) differs from that related to reverse ($\sigma_1 - \rho_{lith}z$) and normal ($\rho_{lith}z - \sigma_3$) faults. Given the same maximum horizontal principal stress at a given depth, the potential of shear failure of wrench faults could be higher than that of reverse and normal faults. Because of their parallelism to lithostatic stress, wrench faults could enhance vertical fracture connectivity and permeability compared with reverse and normal faults under certain geological conditions.

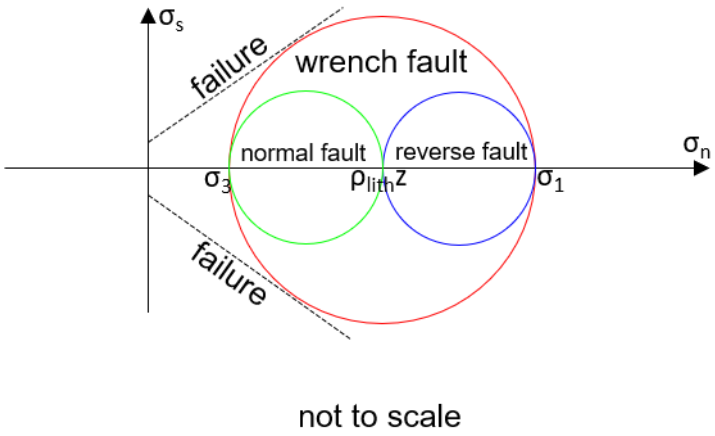


Figure 12. A conceptual model showing distinct principal stress, differential stress, and potential of shear failure of wrench, reverse, and normal faults. The wrench fault stress regime (red) is characterized by vertical intermediate principal stress ($\sigma_2 = \rho_{lith}z$). The normal fault stress regime (green) is characterized by vertical maximum principal stress ($\sigma_1 = \rho_{lith}z$). The reverse fault stress regime (blue) is characterized by vertical minimum principal stress ($\sigma_3 = \rho_{lith}z$). Given a horizontal maximum stress (σ_1), minimum stress (σ_3), and lithostatic stress ($\rho_{lith}z$) at a depth z, the potential

of shear failure, which is represented by the size of the Mohr's circle, is relatively high in the wrench fault stress regime.

4.2. Potential Broad Implications

Bottom-up decompression induced by steep and deep wrench faults could trigger the dissociation, long-distance migration, and emission of methane from subsurface reservoirs, complementing anthropogenic emissions of greenhouse and other environmentally harmful gases released from surface industrial and human activities. Bottom-up hydrothermal heating induced by wrench faults could contribute to the thawing of methane from permafrost and hydrates, complementing top-down feedback of climate change [3,4,22,23]. Given their great penetration depth and areal extent alongside emission efficiency, wrench faults could have played a more important role than other faults in geologic emissions of gases.

The wrench fault causal mechanism of gas emissions can be equally applicable in assessing and mitigating the risk of underground storage through sequestration, often called geologic storage, of greenhouse gases and energy resources in subsurface formations. Geologic storage has long been a popular concept to offset greenhouse gas emissions and to mitigate global environmental change. In structurally complex storage systems in which wrench faults dominate, the environmental risk and operational cost become relevant. Thus, focused investigation and monitoring of wrench faults are instrumental in preventing secondary emissions of sequestered gases.

The wrench fault causal mechanism of gas emissions can be equally applicable in the exploration for and production of energy resources. Wrench faults play a critical role in charging, retaining, and enriching energy resources in energy systems. In petroleum systems, wrench faults present effective migration pathways for oil and gas to flow from sources to reservoirs [10]. In geothermal systems, wrench faults present effective migration pathways for hydrothermal fluids to flow from deep heat sources to shallow hydrothermal reservoirs. In shale gas systems in which shale formations are both sources and reservoirs, wrench faults break the reservoirs, drive gas out of the reservoirs, thus negatively impacting the retention and containment of gases within the reservoirs [31,32].

4.3. Limitations and Future Work

Conceptual modeling in this study is hypothetical, interpretational and qualitative, and the models were developed to explain the possible underlying mechanism of naturogenic gas emissions. My conceptual model, alongside a first-order experimentation (Supplementary Figure S1), was designed and developed to focus on the characterization of wrench faults compared with reverse and normal faults based on the most relevant variables, while keeping other unknown variables constant. In specific cases of natural fault systems, the dynamic process of gas emissions is controlled by numerous variables, which include but are not limited to permeability, aperture, fracture network connectivity, and gas–fault interactions. Gas emissions are also controlled by extrinsic variables such as temperature, formation pressure, confining pressure, pressure gradients, differential stress, and effective normal stress. To characterize real-time dynamic gas flows in wrench, reverse, and normal faults, a geologically meaningful fault/fracture model populated with all the variables that contribute to the flows are required, which remain to be developed in the future.

Environmental integrity and energy security are two pressing yet controversial issues that pose profound societal impacts, whereas wrench faults as a double-edged sword could play a critical role in both emission systems and energy systems. Between the environment and energy, science-based rather than interest-driven research is essential to avoid conflicts of interest and wastes of resources, and to reconcile environment integrity with energy security. Cross-disciplinary research is instrumental in

avoiding extreme biases between protecting the environment and extracting energy at the expense of one another, which will help achieve both environment and energy goals with reduced costs and wastes.

5. Conclusions

It is challenging to partition between anthropogenic and geologic emissions of environmentally harmful gases, and the entire picture of causal mechanisms of environmental changes remains unclear. Integrated subsurface remote sensing and surface monitoring reveal the significance of geologic emissions of environmentally harmful gases and their correlations to wrench faults. Subsurface remote sensing and well bore drilling suggest that wrench faults act as the most effective pathways for methane leaks relative to normal and reverse faults. Surface measurements and dynamic monitoring indicate that radon emission intensity could reach a much higher level on wrench faults relative to reverse and normal faults. Both subsurface and surface data lead to a hypothetic interpretation alongside a conceptual model suggesting wrench faults offer fastest track gas flow pathways due to their unique orientation relative to buoyant force and lithostatic stress. The conceptual model of gas emission systems could be applicable to energy systems as an energy enrichment mechanism. Extensive case studies from the global database will be instrumental in further testing and improving the conceptual model, and all-variable full-order quantitative modeling under realistic geological conditions remains to be further investigated in the future.

Supplementary Materials: The following supporting information can be downloaded at: https://www.mdpi.com/article/10.3390/geosciences16120497/s1, Supplementary Data S1. Worksheet for conceptual modeling of vertical ascent distance z of gas as a function of fault dip α and arrival time t required to reach the surface. Supplementary Data S2. Worksheet for conceptual modeling of instantaneous ascending velocity v of gas as a function of fault dip α. Supplementary Data S3. Worksheet for conceptual modeling of escape time t required for gas to reach the surface as a function of fault dip α. Supplementary Figure S1. First-order experimentation with methane emissions through steep and gentle pathways.

Funding: This research received no federal funding.

Data Availability Statement: All the data relevant to this study are presented in the paper and the supplementary information. Other supporting data are available from the corresponding author upon request.

Acknowledgments: Thanks go to the MDPI Managing Editor for the invitation of the paper. Energy companies provided proprietary 3D seismic data in gas basins worldwide under confidentiality agreements. Marathon Oil, Sinopec, WesternGeco, Schlumberger, Maersk Oil, Occidental Petroleum, Andes Petroleum Ecuador, Energy Corporation of America, and CONSO Energy granted permission to use their seismic data. Sinopec granted 3D seismic, well pressure, and gas production data from the Sichuan Basin. Energy Corporation of America (ECA) provided 3D seismic, well logs, and gas production data from the Appalachian Basin. I am grateful to Sinopec and ECA for their permission for the publications of their proprietary data. Many thanks go to J. Xu, G. Duan, R. Shumaker, T. Wilson, F. Yang, Q. Hu, J. Milliken, T. Evans, L. Seidler, P. Sullivan, W. Zhang, Z. Liu, T. Duan, Z. Feng, M. Li, and R. Holt for their help. A. Sheng and B. Liu assisted with gas emission monitoring and data processing. I am grateful to the editors and three anonymous peer reviewers for their professional comments and constructive suggestions that helped improve the quality of the paper. The author declares no use of Artificial Intelligence (AI) tools for language editing.

Conflicts of Interest: The author declares no conflicts of interest.

References

1. Magnan, A.K.; Pörtner, H.-O.; Duvat, V.K.E.; Garschagen, M.; Guinder, V.A.; Zommers, Z.; Hoegh-Guldberg, O.; Gattuso, J.-P. Estimating the global risk of anthropogenic climate change. *Nat. Clim. Change* **2021**, *11*, 879–885.
2. Shindell, D.T.; Kuylenstierna, J.C.I.; Vignati, E.; van Dingenen, R.; Amann, M.; Klimont, Z.; Anenberg, S.C.; Muller, N.; Janssens-Maenhout, G.; Raes, F.; et al. Simultaneously Mitigating Near-Term Climate Change and Improving Human Health and Food Security. *Science* **2012**, *335*, 183–189.
3. Shindell, D.T.; Faluvegi, G.; Koch, D.M.; Schmidt, G.A.; Unger, N.; Bauer, S.E. Improved attribution of climate forcing to emissions. *Science* **2009**, *326*, 716–718.
4. Zhang, L.; Xia, X.; Liu, S.; Zhang, S.; Li, S.; Wang, J.; Wang, G.; Gao, H.; Zhang, Z.; Wang, Q.; et al. Significant methane ebullition from alpine permafrost rivers on the East Qinghai–Tibet Plateau. *Nat. Geosci.* **2020**, *13*, 349–354.
5. Rocher-Ros, G.; Stanley, E.H.; Loken, L.C.; Casson, N.J.; Raymond, P.A.; Liu, S.; Amatulli, G.; Sponseller, R.A. Global methane emissions from rivers and streams. *Nature* **2023**, *621*, 530–535.
6. Schubert, M.; Paschke, A.; Lieberman, E.; Burnett, W.C. Air−Water Partitioning of ^{222}Rn and its Dependence on Water Temperature and Salinity. *Environ. Sci. Technol.* **2012**, *46*, 3905.
7. Serov, P.; Mattingsdal, R.; Winsborrow, M.; Patton, H.; Andreassen, K. Widespread natural methane and oil leakage from submarine Arctic reservoirs. *Nat. Commun.* **2023**, *14*, 1782.
8. Ostanin, I.; Anka, Z.; Di Primio, R. Role of faults in hydrocarbon leakage in the hammerfest basin, SW barents sea: Insights from seismic data and numerical modelling. *Geoscience* **2017**, *7*, 28.
9. Argentino, C.; Waghorn, K.A.; Vadakkepuliyambatta, S.; Polteau, S.; Bünz, S.; Panieri, G. Dynamic and history of methane seepage in the SW Barents Sea: New insights from Leirdjupet Fault Complex. *Sci. Rep.* **2021**, *11*, 4373.
10. Gao, D. Dynamic interplay among tectonics, sedimentation, and petroleum systems: An introduction and overview. In *Tectonics and Sedimentation: Implications for Petroleum Systems*; Gao, D., Ed.; AAPG Memoir; American Association of Petroleum Geologists: Tulsa, OK, USA, 2012; Volume 100, pp. 1–14.
11. Li, G. *World Atlas of Oil and Gas Basins*; Wiley-Blackwell: Hoboken, NJ, USA, 2011; 496p.
12. EIA. *Technically Recoverable Shale Oil and Shale Gas Resources: An Assessment of 137 Shale Formations in 41 Countries Outside the United States*, 2013 ed.; U.S. Energy Information Administration: Washington, DC, USA, 2013.
13. Gogolak, C.V. *Review of ^{222}Rn in Natural Gas Produced from Unconventional Sources*; DOE/EML-385; U.S. Department of Energy, Environmental Measurements Laboratory: New York, NY, USA, 1980.
14. Ghahremani, D.T. Radon Prospecting for Hydrocarbons—Potential Strategy for Devonian Shale Gas in Northeast Ohio. Ph.D. Dissertation, Case Western Reserve University, Cleveland, OH, USA, 1984.
15. Harrell, J.A.; Belsito, M.E.; Kumar, A. Radon hazards associated with outcrops of Ohio Shale in Ohio. *Environ. Geol. Water Sci.* **1991**, *18*, 17–26.
16. Grossi, C.; Vogel, F.R.; Morguí, J.A.; Curcoll, R.; Àgueda, A.; Batet, O.; Nofuentes, M.; Occhipinti, P.; Vargas, A.; Rodó, X. First estimation of CH_4 fluxes using the ^{222}Rn Tracer Method over the central Iberian Peninsula. In *WIT Transactions on Ecology and the Environment*; WIT Press: Southampton, UK, 2014; Volume 183, pp. 233–244.
17. Mitchell, A.L.; Griffin, W.M.; Casman, E.A. Lung Cancer Risk from Radon in Marcellus Shale Gas in Northeast U.S. Homes. *Risk Anal.* **2016**, *36*, 2105–2119.
18. Tait, D.R.; Santos, I.R.; Maher, D.T.; Cyronak, T.J.; Davis, R.J. Enrichment of Radon and Carbon Dioxide in the Open Atmosphere of an Australian Coal Seam Gas Field. *Environ. Sci. Technol.* **2013**, *47*, 3099–3104.
19. Wysocka, M. Radon in the investigations of geo-hazards in Polish collieries. *Geofluids* **2010**, *10*, 564–570.
20. Sarkar, S.; Berndt, C.; Minshull, T.A.; Westbrook, G.K.; Klaeschen, D.; Masson, D.G.; Chabert, A.; Thatcher, K.E. Seismic evidence for shallow gas-escape features associated with a retreating gas hydrate zone offshore west Svalbard. *J. Geophys. Res. Solid Earth* **2012**, *117*, B09102.
21. Berndt, C. Temporal Constraints on Hydrate-Controlled Methane Seepage off Svalbard. *Science* **2014**, *343*, 284–287.
22. Ketzer, M.; Praeg, D.; Rodrigues, L.F.; Augustin, A.; Pivel, M.A.G.; Rahmati-Abkenar, M.; Miller, D.J.; Viana, A.R.; Cupertino, J.A. Gas hydrate dissociation linked to contemporary ocean warming in the southern hemisphere. *Nat. Commun.* **2020**, *11*, 3788.
23. Davies, R.J.; Yang, J.; Ireland, M.T.; Berndt, C.; Maqueda, M.Á.M.; Huuse, M. Long-distance migration and venting of methane from the base of the hydrate stability zone. *Nat. Geosci.* **2024**, *17*, 32–37.
24. Skarke, A.; Ruppel, C.; Kodis, M.; Brothers, D.; Lobecker, E. Widespread methane leakage from the sea floor on the northern US Atlantic margin. *Nat. Geosci.* **2014**, *7*, 657–661.

25. Ketzer, M.; Praeg, D.; Augustin, A.H.; Rodrigues, L.F.; Steiger, A.K.; Rahmati-Abkenar, M.; Viana, A.R.; Miller, D.J.; Malinverno, A.; Dickens, G.R.; et al. Gravity complexes as a focus of seafloor fluid seepage: The Rio Grande Cone, SE Brazil. *Sci. Rep.* **2023**, *13*, 4590.
26. Panieri, G.; Knies, J.; Vadakkepuliyambatta, S.; Lee, A.L.; Schubert, C.J. Evidence of Arctic methane emissions across the mid-Pleistocene. *Commun. Earth Environ.* **2023**, *4*, 109.
27. Newman, K.R.; Cormier, M.-H.; Weissel, J.K.; Driscoll, N.W.; Kastner, M.; Solomon, E.A.; Robertson, G.; Hill, J.C.; Singh, H.; Camilli, R.; et al. Active methane venting observed at giant pockmarks along the U.S. mid-Atlantic shelf break. *Earth Planet. Sci. Lett.* **2008**, *267*, 341–352.
28. Andresen, K.J.; Huuse, M.; Clausen, O.R. Morphology and distribution of Oligocene and Miocene pockmarks in the Danish North Sea–implications for bottom current activity and fluid migration. *Basin Res.* **2008**, *20*, 445–466.
29. Chand, S.; Rise, L.; Ottesen, D.; Dolan, M.; Bellec, V.; Bøe, R. Pockmark-like depressions near the Goliat hydrocarbon field, Barents Sea: Morphology and genesis. *Mar. Pet. Geol.* **2009**, *26*, 1035–1042.
30. Pau, M.; Hammer, O.; Chand, S. Constraints on the dynamics of pockmarks in the SW Barents Sea: Evidence from gravity coring and high-resolution, shallow seismic profiles. *Mar. Geol.* **2014**, *355*, 330–345.
31. Gao, D.; Roberts, E.; Geiger, C.; Sullivan, P. Acadian detachment and wrench faults in central Pennsylvania: Implications for the Marcellus Shale reservoir integrity and gas productivity in the hinge of the Pennsylvania Salient. *Interpretation* **2020**, *8*, T151–T165.
32. Gao, D.; Duan, T.; Wang, Z.; Shang, X. Caledonian detachment deformation and deposition in the Fuling gas field of the southeastern Sichuan Basin in China: Implications for the Lower Silurian Longmaxi Shale gas exploration and production. *Interpretation* **2018**, *6*, SN119–SN132.
33. Kulander, B.R.; Dean, S.L. Structure and tectonics of central and southern Appalachian Valley and Ridge and Plateau Provinces, West Virginia and Virginia. *Am. Assoc. Pet. Geol. Bull.* **1986**, *70*, 1674–1684.
34. Faill, R.T. A geologic history of the north-central Appalachians, part 1, Orogenesis from the Mesoproterozoic through the Taconic Orogeny. *Am. J. Sci.* **1997**, *297*, 551–619.
35. Wheeler, R.L. Cross-strike-structural discontinuities: Possible exploration tool for natural gas in Appalachian overthrust belt. *AAPG Bull.* **1980**, *64*, 2166–2178.
36. Gao, D.; Shumaker, R.C.; Wilson, T.H. Along-axis segmentation and growth history of the Rome trough: Central Appalachian basin. *AAPG Bull.* **2000**, *84*, 75–99.
37. Sak, P.B.; Gray, M.B.; Ismat, Z. Significance of the deformation history within the hinge zone of the Pennsylvania Salient, Appalachian Mountains. *J. Geol.* **2014**, *122*, 367–379.
38. Kulander, C.S. *Regional Seismic Lines in West Virginia-a Preliminary Look at the Rome Trough and Its Implications for Energy Resources*; Open-File Report; U.S. Geological Survey: Reston, VA, USA, 2001.
39. Engelder, T.; Lash, G.G.; Uzcátegui, R.S. Joint sets that enhance production from Middle and Upper Devonian gas shales of the Appalachian Basin. *AAPG Bull.* **2009**, *93*, 857–889.
40. Lash, G.G.; Engelder, T. Thickness trends and sequence stratigraphy of the Middle Devonian Marcellus Formation, Appalachian Basin: Implications for Acadian foreland basin evolution. *AAPG Bull.* **2011**, *95*, 61–103.
41. Zagorski, W.A.; Wrightstone, G.R.; Bowman, D.C. The Appalachian Basin Marcellus gas play: Its history of development, geologic controls on production, and future potential as a world-class reservoir. In *Shale Reservoirs–Giant Resources for the 21st Century*; Breyer, J.A., Ed.; AAPG Memoir; American Association of Petroleum Geologists: Tulsa, OK, USA, 2012; Volume 97, pp. 172–200.
42. Shultz, C.H. *The Geology of Pennsylvania*; Schultz, C., Ed.; Pennsylvania Geological Survey Special Publication; Pennsylvania Geological Survey and Pittsburgh Geological Society: Harrisburg, PA, USA, 1999; Volume 1, pp. 286–297.
43. Kuhn, O. Ancient Chinese Drilling. *CSEG Rec.* **2004**, *29*, 1–15.
44. Ryder, R.; Rice, D.; Sun, Z.; Zhang, Y.; Qiu, Y.; Guo, Z. *Petroleum Geology of the Sichuan Basin/China–Report on U.S. Geological Survey and Chinese Ministry of Geology and Mineral Resources Field Investigations and Meetings, October 1991*; Open-File Report 94-426; U.S. Geological Survey: Reston, VA, USA, 1994; 67p.
45. Dai, J.X.; Zou, C.; Liao, S.; Dong, D.; Ni, Y.; Huang, J.; Wu, W.; Gong, D.; Huang, S.; Hu, G. Geochemistry of the extremely high thermal maturity Longmaxi shale gas, southern Sichuan Basin. *Org. Geochem.* **2014**, *74*, 3–12.
46. Guo, T. The Fuling Shale Gas Field–A highly productive Silurian gas shale with high thermal maturity and complex evolution history, southeastern Sichuan Basin, China. *Interpretation* **2015**, *3*, SJ25–SJ34.
47. Sun, J.; Luo, B. Structural deformation and its influences on gas storage in Fuling shale gas play, the Sichuan Basin. *Oil Gas Geol.* **2016**, *37*, 809–818.

48. Guo, X.; Hu, D.; Wei, X.; Li, Y. Major factors controlling shale fractures and their influences on production capacity in Jiaoshiba area, the Sichuan Basin. *Oil Gas Geol.* **2016**, *37*, 799–808.
49. Ma, Y.; Fan, M.; Lu, Y.; Guo, X.; Hu, H.; Chen, L.; Wang, C.; Liu, X. Geochemistry and sedimentology of the Lower Silurian Longmaxi mudstone in southwestern China: Implications for depositional controls on organic matter accumulation. *Mar. Pet. Geol.* **2016**, *75*, 291–309.
50. Liu, Y.; Liao, R.; Zhang, Y.; Gao, D.; Zhang, H.; Li, T.; Zhang, C. Application of surface–downhole combined microseismic monitoring technology in the Fuling shale gas field and its enlightenment. *Nat. Gas Ind. B* **2017**, *4*, 62–67.
51. Lei, X.; Huang, D.; Su, J.; Jiang, G.; Wang, X.; Wang, H.; Guo, X.; Fu, H. Fault reactivation and earthquakes with magnitudes of up to Mw 4.7 induced by shale-gas hydraulic fracturing in Sichuan Basin, China. *Sci. Rep.* **2017**, *7*, 7971.
52. Li, J.; Xu, J.; Zhang, H.; Yang, W.; Tan, Y.; Zhang, F.; Meng, L.; Zang, Y.; Miao, S.; Guo, C.; et al. High seismic velocity structures control moderate to strong induced earthquake behaviors by shale gas development. *Commun. Earth Environ.* **2023**, *4*, 188.
53. Gao, D.; Duan, G.; Sheng, A.; Wang, Y. Tectonic setting and underlying mechanism of latent geologic hazards in Shanghai and its adjacent areas, China. *Shanghai Geol.* **1990**, *11*, 1–8. (In Chinese with English Abstract)

Disclaimer/Publisher's Note: The statements, opinions and data contained in all publications are solely those of the individual author(s) and contributor(s) and not of MDPI and/or the editor(s). MDPI and/or the editor(s) disclaim responsibility for any injury to people or property resulting from any ideas, methods, instructions or products referred to in the content.